Re: <u>Authors Reply to Review nhess-2021-280</u>

Dear reviewer,

We would like to thank you for reviewing our paper, *"Ground motions variability in Israel from 3-D simulations of M 6 and M 7 earthquakes"* (*nhess-2021-280*).

Thank you for the time spent and the positive attitude towards this work. Your remarks and critique certainly improved the manuscript.

Attached below is our pointwise reply to the general and specific comments. All the changes and additions are marked in the revised version of the manuscript.

All the co-authors approved the revision. Please address all correspondence to:

Jonatan Glehman

Department of Earth and Environmental Sciences
Ben Gurion University of the Negev
Beer-Sheva 8410501
Israel.

(glechman@post.bgu.ac.il)

Referee comments for manuscript nhess-2021-280 titled "Ground motions variability in Israel from 3-D simulations of M6 and M7 earthquakes", by Jonatan Glehman and Michael Tsesarsky

General comments

The manuscript describes a study of ground motion variability associated with simulations of 3D ground motions from M7 and M6 earthquakes, along major seismogenic sources in Israel. The authors use a 3-D model of the sub-surface that describes the main features of the spatial heterogeneity in Israel and simulate the ground motions at 129 measurement locations in the northern part of Israel. Then the authors derive a statistical attenuation model based on the simulations, and analyse the residuals, single station variability and significant durations.

This is of importance to low-moderate seismicity regions, and specifically to Israel. Complementing the instrumental catalogue with simulated strong ground motions is important, as well as understating and evaluating the variability associated with the simulated ground motions.

Specific comments

Why is there no subfigure for the minimization of the residuals to all 3 predictor variables in Figure S3 for magnitude 6?

Reply: For M6, Z_2 has a minimal impact on the residual's standard deviation (<0.001), therefore we decided to not include it as an explanatory variable (please refer to table 4 and lines 406-408 on page 18); Hence, there was no subfigure for Z_2 in figure S3 for M 6.

However, to clarify this point further, we followed your suggestion and added the quantitative impact of Z_2 on M 6 and the impact of Z2 on the minimization of the total residuals in Figure S3 (a,c and e). Thank you. Please refer to lines 404 - 407 in the revised manuscript.

When comparing the simulations to CB14 – can the authors elaborate as to the predictor variable values used in CB14? Did they use 608 m/s for Vs30?

Reply: Thank you for this comment. The CB-14 PGVs were calculated for a strike-slip fault, where we used the surface shear wave velocity as the Vs30 parameter input for CB-14 (this is due the minimum grid spacing of 76 meters). The Basin response term Z_2 in our model is analogue to $Z_{2.5}$ in CB-14. The Magnitude term was calculated according to the simulated magnitudes; Mw 6.21 and Mw 6.85. We added this information and an example of CB-14 GMM to Figure 5 to clarify this point further, please refer to lines 270 – 271 (Figure 5. Caption) and 337-339 in the revised manuscript.

It seems like the AM over-predicts GM at the sedimentary wedge rupture distances (Figure 9), can the authors comment on that? It would seem that most of the data at these distances is lower, and will result in a lower model that under-predicts.

> **Reply:** Thank you for this valuable comment. The residuals between the simulated and AM (mean PGVs in Figures 7 and 8 show that, except for stations 18 and 17 (located on the edge of the Sedimentary wedge), the AM under-predicts the ground motions at the Sedimentary wedge. Thus, the contribution to the AM's over-prediction comes from other sites located at these distances. As mentioned on page 15, lines: 348-351, the residuals were computed as a moving average over distance. Thus, they are independent of site-specific terms.

Lines 354 – 363: I really don't see this in the data. I don't see the triangles lower than the squares, and it is very difficult to tell them at all from the other symbols. I suggest thinking of a clearer way to present the data, as presently the figure does not support the statements in the text.

> **Reply:** Thank you for pointing it out. We modified figure 10 to support the text in the lines mentioned above.

In lines 389 – 391, the authors state that the AM couldn't capture the full site effects of the Zevulun Valley and the sedimentary wedge, and further model refinements are required. Do the authors think that such effects can be incorporated successfully into a regional GMM?

> **Reply:** This is a challenging question. We do believe that such effects could be incorporated into a regional GMM. We are currently studying additional terms; unique to the Zevulun Valley and the Sedimentary wedge, such as $Z_{0.8}$ as well as distance-dependent and rupture velocity-dependent attenuation terms, for directivity and super-shear ruptures, among others. We added this information to the revised manuscript. Please refer to lines 462 - 464.

Technical corrections

The acronyms GMM and GMPE are used throughout the manuscript, please select one and be consistent.

> **Reply:** Thank you for this comment. We changed all acronyms to GMM.

The past and present tense are used interchangeably to describe what is / was done. Please select one and be consistent.

> **Reply:** Corrected. Thank you.

Line 70 – what is a magnitude limited GMPE? Unclear. Please explain.

> **Reply:** Explained. Thank you.

Line 93: Israel should be Israeli.

> **Reply:** Corrected. Thank you.

Line 93: ranges should be range.

> **Reply:** Corrected. Thank you.

Figure 1 caption (lines 121, 123): I think it should say Israel seismic network **stations**.

> **Reply:** Corrected. Thank you.

Line 135: "the Israeli coastal plain**,** " - the comma is missing, and the word "is" should be deleted.

> **Reply:** Corrected. Thank you.

Line 143: delineate rather than delimit.

> **Reply:** Corrected. Thank you.

Lines 159 – 166: the word rupture is misspelled many times.

> **Reply:** Corrected. Thank you.

Line 179: "ground motion**s** records"- the 's' should be deleted.

> **Reply:** Corrected, line 181. Thank you.

Line 182: the sentence "we developed the regional velocity model of Shimony et al (2021) is unclear. If the model is Shimony et al.'s – then it wasn't developed by the authors. If it is a modification, or based on their results, then please explain what was done.

> **Reply:** Thank you for highlighting this point. The model of Shimony et al., was refined and expanded. We added this information to the text, lines 184-186 in the revised manuscript.

Line 183: the word "following" here seems awkward. Please consider rephrasing.

> **Reply:** Corrected, line 186. Thank you.

Line 185 – "statistical analysis **of** the synthetic database".

> **Reply:** Corrected, line 188. Thank you.

Line 203: in the Gvirtzman et al. quote the comma should be deleted. Also, the capital T in The Zevulun Valley is unnecessary.

> **Reply:** Corrected, line 208. Thank you.

Line 255: station 123 is not visible in Figure S1.

> **Reply:** Thank you for pointing it out. We added station 123 to Figure S1.

Line 281 – it seems like there should be a better way to start a sentence than "Following, ". Perhaps: "We then examine the simulated…".

> **Reply:** Corrected, line 290. Thank you.

Page 14 – Fig. 6 – it seems that the SF scenario is missing from the figure altogether but referred to in the text. This is also true for figure 5. I also recommend that in the captions of figures 5 and 6 the abbreviations of the faults and source characteristics be explained again.

> **Reply:** Thank you for this comment. The SF (Shemona fault) scenario appears in figures 5 and 6 for M 7 scenarios. We did not model this scenario for M 6. Please refer to Table 3. We added additional description to these figures, as suggested, lines 266-268 (figure 5) and lines 314-316 (figure 6).

Line 299: the trade off sentence is a bit unclear (what trades off here). I suggest adding: ".... between the ground motion intensity in the Zevulun Valley (triangles) and the *ground motion intensity* in the Sedimentary wedge….".

> **Reply:** Modified. Thank you, see lines 306-313.

Line 300 – a comma is missing before "…in an asymmetric rupture…"

> **Reply:** Added, line 307. Thank you.

Figure 7 – the color bar of the mean peak ground velocity isn't very visible, I advise you to pick different colors, and make them vivid, say green – yellow – orange- red. Right now it is very difficult to observe the colors. Also, since you give just two locations as examples (station 129 and stations 127), it would be more convenient to identify these in the figure, rather than refer to a figure in the supplementary material.

> **Reply:** We modified the color bar and added stations 127 and 129 to the figure. Thank you.

Lines 369-375: this paragraph seems more suited to a summary section.

> **Reply:** Thank you for the suggestion. We believe that this paragraph contributes to the flow of the discussion and is an integral part of it. However, we renamed the section to "discussion and summary".

Line 399: the word is is missing: "noteworthy to mention **is** that…."

> **Reply:** Added, line 424. Thank you.

Line 404: when using the GMM acronym, the word model is redundant.

> **Reply:** Corrected, line 430. Thank you.

Line 406: define IM.

> **Reply:** Definition added, lines 170-171. Thank you.

Line 419: "four simulated ground motion**s** datasets" – the s of the plural for ground motion should be omitted.

> **Reply:** Corrected, line 448. Thank you.

Ground motions variability in Israel from 3-D simulations of M 6 and M 7 earthquakes

Jonatan Glehman[1] and Michael Tsesarsky[1,2]

[1]Department of Earth and Environmental Sciences, Ben Gurion University of the Negev, 8410501, Israel
[2]Department of Civil and Environmental Engineering, Ben Gurion University of the Negev, 8410501, Israel

Correspondence to: Jonatan Glehman (glechman@post.bgu.ac.il)

Abstract. In Israel, due to low seismicity rates and sparse seismic network, the temporal and spatial coverage of ground motion data is insufficient to estimate the variability of moderate-strong (M > 6) ground motions required to construct a local ground motion model (GMM). To fill this data gap and to study the ground motions variability of M > 6 events, we performed a series of 3-D numerical simulations of M 6 and M 7 earthquakes. Based on the results of the simulations, we developed a parametric attenuation model (AM) and studied the residuals between simulated and AM PGVs and the single station variability. We also compared the simulated ground motions with a global GMM in terms of peak ground velocity (PGV) and significant duration (Ds 595). Our results suggested that the AM was unable to fully capture the simulated ground motions variability, mainly due to the incorporation of super-shear rupture and effects of local sedimentary structures. We also showed that an imported GMM considerably deviates from simulated ground motions. This work sets the basis for future development of a comprehensive GMM for Israel, accounting for local sources, path, and site effects.

1   Introduction

The recent report by the Centre for Research on the Epidemiology of Disasters (CRED) and the UN Office for Disaster Risk Reduction (UNDRR) – Human Cost of Disasters, 2000 - 2019 – clearly shows that earthquakes are the deadliest natural disasters. accounting for only 3 % of the total number of people affected by natural disasters, they count for 58 % of deaths (more than 700,000) of all disaster types and 21 % of recorded economic losses (Mizutori and D'ebarati, 2020). Over the past 40 years, the global population exposed to a moderate to severe intensity earthquake has increased by 93 % (to 2.7 billion people) (Pesaresi et al., 2017). This value is expected to grow with population growth and increasing urbanization.

Seismic hazard is the intrinsic natural occurrence of earthquakes and the resulting ground motion and other effects (Wang, 2005). Ground motion models (GMM's) are critical components in the mitigation of seismic hazard. Empirically based GMMs, also known as Ground Motion Prediction Equations (GMPE's), are parametric models that estimate the median and the variability of the expected ground motions at a site. The main explanatory variables of such models are typically earthquake magnitude, distance, and site conditions. New generation GMMs also address faulting style, depth to rock, and others.

Many regions worldwide, either due to low seismicity rates and/or sparse coverage of the seismic network, do not provide sufficient temporal and spatial data to estimate the variability of ground motions required to construct a local GMM or validate an imported GMM to local conditions. This situation is specifically acute in the range of strong earthquakes at relatively short distances that pose the most significant hazard to human life and infrastructure.

The use of imported GMM's under the ergodic assumption attributes the ground motion variability to the randomness of the process (i.e., aleatory variability) rather than to local systematic source-path and site effects (i.e., epistemic uncertainty) (Anderson and Brune, 1999). Abrahamson et al., (2019) showed that the increased number of strong-motion records over the past decade exhibit significant differences in scaling of the ground motions even within relatively small regions and that most of the variability typically treated as aleatory is actually due to systematic source, path, and site effects. Kuehn et al., (2019) showed the importance of variations in quality factor (Q) over small spatial scales (30 km) in California. Specifically showing that accounting for path effects leads to a smaller value of the aleatory variability and results in different median predictions, depending on source and site location. To achieve this improvement, Kuehn et al., (2019) divided California into a grid with a cell size of 30 km by 30 km and used 12,039 records from 274 events recorded at 1504 stations. This approach can be employed only in data-rich regions, such as California. Lan et al., (2019) showed that for South Western China, imported GMM's result in significant discrepancies compared with regional instrumental data (including the Wenchuan Mw 7.9 event). In addition, despite the recorded ground motion data expanding, it remains sparse for large, complex ruptures with recurrence intervals generally exceeding the observation length of instrumental records.

The challenges met while predicting ground motion in data-poor regions turn numerical modeling into an essential complementary method for seismic hazard analysis (Chaljub et al., 2010). Numerical modeling alleviates the need for the ergodic assumption, as it can augment the seismic data with strong motion records and account for ground motions variability by systematically separating source, path, and site effects. For example, Graves et al., (2011) showed that the combination of rupture directivity and basin response effects could lead to an increased hazard in particular sites, relative to that calculated by GMM. Pitarka et al., (2021) found that the combination of rupture propagation effects with the amplification due to local topography can result in large ground motions amplifications with complex spatial variability.

However, the shift from ergodic models to nonergodic models, which account for local source-site and path effects such as numerical models, leads to large epistemic uncertainty in the median ground motion, resulting in increased epistemic uncertainty of the hazard (Walling and Abrahamson, 2012). Such uncertainty is derived from both modeling and parametric uncertainties, as the model, is not well constrained. Model uncertainty can be reduced by using more accurate 3D crustal models and source models.

Subsurface models with different levels of accuracy and completeness are available around the world. With the increasing use of terrestrial and space geodesy, the control of seismic sources is also improving with time. Combining the two enables the construction of numerical models for regional assessment of ground motions (Pitarka et al., 2021; Douglas and Aochi, 2008; Graves and Pitarka, 2015). A hybrid GMM, based on empirical and synthetic ground motion databases, is expected to reduce the epistemic uncertainty of the median ground motion and will lead to a lower aleatory variability than GMM's based on data with limited magnitude and distance bands.

In Israel, low seismicity rates (centennial and millennial return periods) and a limited instrumental catalog, spanning only four decades and contain mainly M < 6 events, impede the development of local empirical GMM. The practical outcome of this shortcoming is the use of imported GMM's, such as the Campbell & Bozorgnia, (2008) used in the Israel Seismic Design Code IS 413 (Israel Standards Institution, 2013). Contrary to the

76 instrumental catalog, the Israel pre-instrumental catalog spans over three millennia (Agnon, 2014), including

77 numerous M > 6 events, with up to 14 M > 7 events.

78   This paper presents numerical modeling of ground motions in Israel, intended to narrow the strong ground

79 motion data gap and study ground motions variability from moderate (M 6) and strong (M 7) earthquakes. We

80 begin with a brief introduction to the seismo-tectonic setting of the region. Then, we proceed to the methodology

81 section to describe the process of generating a synthetic ground motion database and the subsequent construction

82 of a parametric ground motion model. The results section presents the simulated ground motions and the respective

83 attenuation model. Then, it compares it with the global GMM's of Campbell & Bozorgnia, (2014; hereafter,

84 CB14) and Afshari & Stewart, (2016) performance with respect to the synthetic database. Finally, we discuss our

85 findings and provide insights regarding the seismic hazard from moderate to strong earthquakes and the

86 importance of developing a comprehensive regional GMM to mitigate the seismic hazard in Israel.

87 ## 2   The seismo-tectonic setting of Israel

88 ### 2.1   Seismicity and seismic hazard in Israel

89 The Dead Sea Transform (DST) fault system is an active tectonic boundary separating the African and Arabian

90 plates. Extending from the Gulf of Aqaba to southern Turkey, a total length of approx. 1100 km, it dominates the

91 seismicity of Israel, Palestinian Authority, Lebanon, and Syria (Fig. 1a,b). The DST is a left-lateral strike-slip

92 fault with a total offset of 105 km (Garfunkel, 2014). The average long-term slip rate is 4 to 5 mm year^{-1} (Bartov

93 et al., 1980). Geodetic slip rates along the Israeli part of the DST range from 3 to 5 mm year^{-1} (Hamiel et al., 2016;

94 Sadeh et al., 2012).

95   Splaying north-west from the DST is the Gilboa Fault, and farther north-west towards the Mediterranean,

96 the Carmel Fault. Both comprise an active zone generalized as the Carmel Fault Zone (CFZ). The DST segments

97 are capable of producing M 6 and M 7 events (Shamir et al., 2001), and the CFZ is capable of producing up to M

98 6.5 earthquakes (Grünthal et al., 2009).

99   The Israel Seismic Network (ISN), established in 1983 and upgraded over the years, consists of a mixture

100 of different instrumental and operational stations, including short-period stations (24 in total), broadband stations

101 (14 in total), and a large broadband array (part of the Comprehensive Nuclear Test Ban Treaty). The deployment

102 of the ISN does not cover areas of increased seismic hazard, e.g., densely populated zones and soil sites, or areas

103 designated by the Israel Seismic Code (IS413) as suspected in extreme ground motion amplification, such as the

104 Zevulun Valley (Fig. 1b). Currently, the seismic network is upgraded within the Tru'a project (an early warning

105 system), with up to 60 strong-motion accelerometers and 12 broadband seismometers added to ISN (Kurzon et

106 al., 2020). However, most of the instrumentation are placed along the DST and Carmel fault to provide early

107 warning, and not in densely populated or industrialized areas where the seismic risk is tangible. Based on

108 demographic projections (the Taub Center for Social Policy Study in Israel; For URL see data and resources) the

109 population of Israel is expected to grow from 9.05 million in 2021 to 12.8 million in 2040 and combined with the

110 increasing demand for housing and infrastructures, the seismic risk is expected to grow.

111   The Israel seismic catalog covers 36 years of measurements (1985–2021) and includes more than 23,300

112 events (Wetzler & Kurzon,2016), but only 15 of them are of M > 5 (Fig. 1a and Fig. 2). Moving back in time,

113 Israel's pre-instrumental catalog spans over 3000 years (Agnon, 2014; Zohar, 2019) with many catastrophic

114   events, such as the 749 (M > 7), 1202, (M > 7.5), 1759 (M > 7), and the 1837 (M >7) earthquakes, among others.

115   In total, fourteen M > 7 events were cataloged by Ambraseys (2006) in the past two millennia. Recent geodetic

116   studies (Hamiel et al., 2016; Sadeh et al., 2012) identified a slip deficit on specific segments of the DST, such as

117   the Jordan Gorge Fault (JGF) and the Jordan Valley Fault (JVF), equivalent to an M > 7 earthquake.
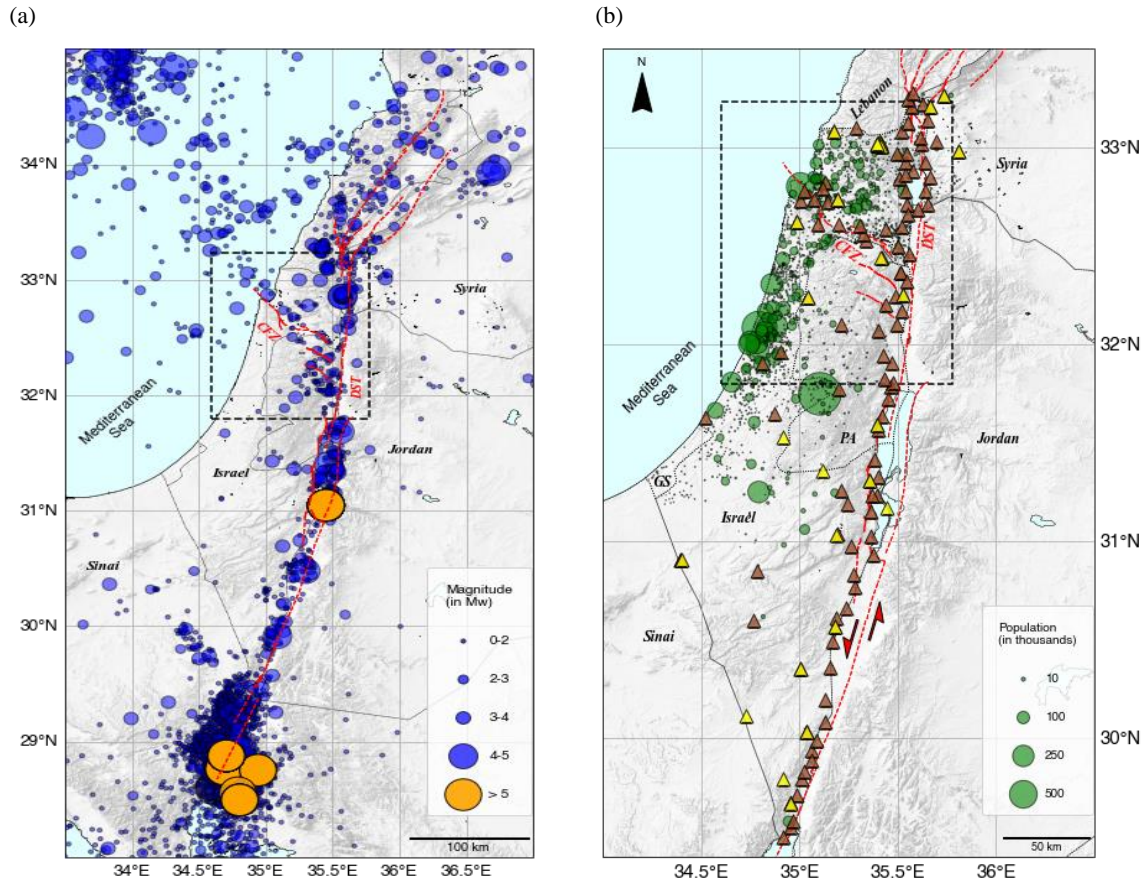
118   **Figure 1.** (a) Israel Seismic catalog (Mw) for the period 1985-2021 orange circles are events with Mw > 5 (expansion of

119   Wetzler & Kurzon (2016) catalog). Red lines are active tectonic borders and faults, DST is Dead Sea Transform, CFZ is

120   Carmel Fault Zone. (b) Demographics of Israel and the Palestinian Authority and the deployment of the Israel Seismic

121   Network. Yellow triangles are the old (up to October 2017) Israel Seismic network stations, brown triangles are the current

122   (Tru'a) seismic network stations. (after Kurzon et al., (2020)). GS is Gaza Strip. The black rectangles define the computational

123   domain presented in Fig. 3a.
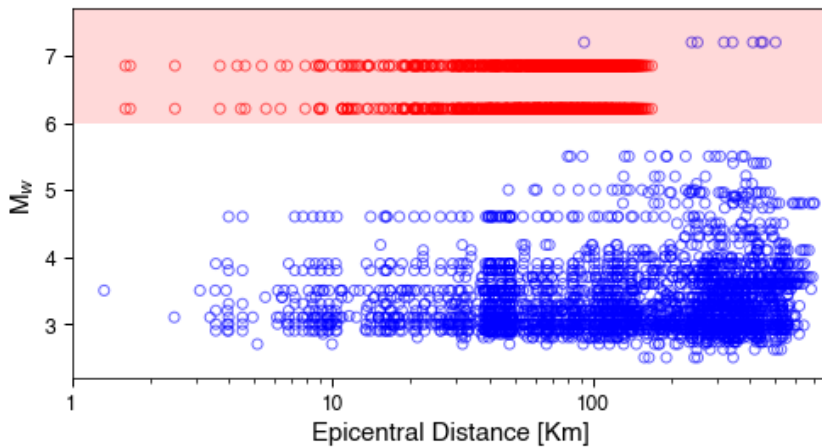
Figure 2. Israel's ground motion database (blue circles) for the period 1983-2021 as a function of epicentral distance (Yagoda-Biran et al., 2021). The shaded rectangle spans the Mw > 6 region of moderate-strong ground motion records. The red circles are the simulated ground motions from this work.

2.2 Spatial heterogeneity of Israel

The geological structure of Israel exhibits strong spatial heterogeneity over short scales (Fig. 3a,b). Deep pull-apart basins (up to 10 km) filled with soft sediments (Vs ~ 600-800 m sec^{-1}) accompany the active DST system, from south to north: The Dead Sea Basin, Beit Shean Valley (BSV), the Sea of Galilee (SG) and the Hula Valley. Along the CFZ, the Zevulun, Harod, and Jezreel Valleys are formed. The vulnerability of Zevulun Valley is particularly crucial because of its dense population and the high concentration of strategic industrial infrastructure (Shani-Kadmiel et al., 2020).

The Israeli coastal plain, one of the most densely populated regions of the country (on average, 9000 people per km^2), is underlain by a westward thickening sedimentary wedge (SW). In the Judea foothills area, east of the SW, a strong reflector exists between the sandstones and clays (Pleistocene Kurkar Gr, Vs ~ 300 m sec^{-1}) and the hard carbonate rocks (the Cretaceous Judea Gr., Vs ~ 2000 m sec^{-1}). In the coastal plain, the Kurkar Gr. overlays the soft carbonates (Avedat Gr, Vs ~ 900 m sec^{-1}) and clastic sediments (the Bet Guvrin Fm., Vs ~ 800 m sec^{-1}) (refer to Fig. 3b). The depth of the Kurkar Gr. base reflector is typically several tens of meters. Further to the west, a prominent reflector is a contact between the clays (Pliocene Yafo Fm., Vs ~ 600 m sec^{-1}) and top of Judea Gr. These two reflectors, when shallower than 250 m, were used for the latest update of the Israel Building Code IS 413 (Israel Standards Institution, 2013) to delineate areas of high potential of ground motion amplification (Gvitzman and Zaslavsky, 2009). This situation further complicates the process of developing an empirical GMM for Israel.

2.3 Source effects

The impact of inter-basin sources along the DST on regional ground motions was examined by Shimony et al., (2021). This work clearly showed that regional ground motions are determined by source-path coupling effects in the strike-slip basins before waves propagate into the surrounding areas. Ground motions are determined by the location of the rupture nucleation, the near-rupture lithology, and the local structures. Shimony et al., focused on symmetric sub-shear ruptures and did not model rupture directivity or super-shear rupture velocities, both known to amplify regional ground motions.

153 Under specific conditions, super-shear ruptures and directivity occur on bi-material faults (Shi & Ben-Zion
154 2006). Specifically, for subsonic propagation, symmetrically initiated bilateral rupture evolves after some
155 propagation distance to a unilateral rupture in the positive direction, which is the direction of slip on the compliant
156 side of the fault containing the softer layer. The magnitude of this effect increases with propagation velocity and
157 the degree of material contrast across the fault. At super-shear propagation speeds, along a bi-material fault, the
158 propagation direction is reversed.

159 The DST is a mature left-lateral fault with a 105 km offset, resulting in strong material contrast between
160 the hard layers on the Jordan side (east) and the soft layers on the Israeli side (west). Thus, the rupture can
161 potentially propagate unilaterally southwards, discharging most of the seismic energy into Israel or northward in
162 super-shear mode. The Jordan Gorge Fault and the Jordan Valley Fault (both active faults of the DST) specifically
163 can produce an earthquake with rupture propagating in super-shear velocity since they border deep sedimentary
164 basins, characterized by large shear wave velocities contrast along the rupture propagation path. Thus, to quantify
165 the seismic hazard ensuing from bi-material faults, it is necessary to study the two propagation directions; both
166 sub-shear and super-shear velocities.

167 The primary purpose of this study is to examine different source, path, and site effects of simulated,
168 moderate M 6 and moderate-strong M 7 earthquakes and their contribution to ground motion variability. To this
169 end, we simulated M 6 and M 7 earthquakes with different source and path properties. Then, we developed a
170 parametric representation of median ground motions and their variability. Formulated in terms of a single ground
171 motion intensity measure (IM), Peak Ground Velocity (PGV), our model quantifies the spatial distribution of the
172 ground motions in central and northern Israel, accounting for local source, path, and site effects, including rupture
173 velocity and directivity.
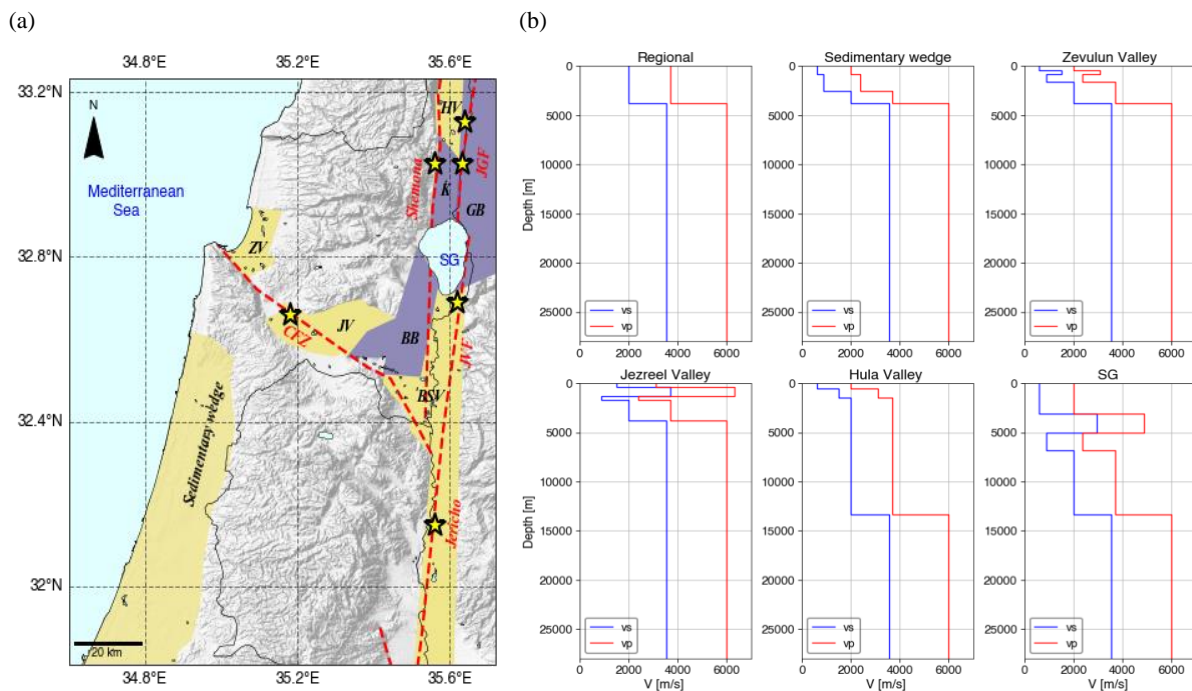
174 **Figure 3.** (a) The DST fault system and the Carmel Fault Zone (CFZ) and accompanying structures. Sedimentary structures
175 (yellow): BSV-Beit Shean Valley, ZV-Zevulun Valley, JV-Jezreel Valley, HV-Hula Valley, SG-Sea of Galilee, and the
176 Sedimentary wedge; and hard rock structures (purple): K-Korazim structural saddle, BB-Belvoir Basalts, GB-Golan Basalts.

177 The yellow stars indicate the epicenter of the seismic sources simulated in our work: Jordan Gorge Fault (JGF), with bilateral
178 and unilateral slip realization, Jordan Valley Fault (JVF), Jericho Fault, Shemona Fault (only for M 7), and CFZ (only for M
179 6). (b) Representative depth velocity profiles of the computational domain.

3   Methodology and workflow

181 Developing a regional GMM for Israel requires a database of ground motion records, including M > 6 events at
182 short, <100 km, distances. To supplement the existing ground motions database, we added a suite of synthetic
183 ground motions from physics-based 3D numerical models of different M 6 and M 7 earthquakes (Fig. 2).
184   Our work comprised two main stages; first, we modified and expanded the regional velocity model of
185 Shimony et al., (2021), to represent a more realistic geological setting and contain the Golan Basalts, the central
186 part of Israel, and the sedimentary wedge. Then, we simulated five different earthquake scenarios for each
187 magnitude, with nucleation at different locations along the DST and CFZ. For each scenario, we recorded synthetic
188 ground motions at 129 stations (see supplementary material, Fig. S1). Next, we performed statistical analysis of
189 the synthetic database, using multivariable regression, by minimizing residuals between data and model
190 estimations. We then formulated a parametric model of the ground motions and examined its consistency with the
191 simulated database, in terms of the median ground motions and their variability for each of the simulated scenarios.

3.1   Numerical model

193 Ground motions in this research were modeled using the SW4v2 software (Petersson and Sjogreen, 2014, 2017a,
194 b), developed for large-scale simulations of seismic wave propagation on parallel computers.
195   The velocity model covers the northern and central part of Israel (fig. 4a) and includes the main DST trough
196 and the following basins/structures, from south to north: Beit Shean Valley (BSV), Belvoir Basalts (BB), Sea of
197 Galilee (SG), Korazim structural saddle (K), Golan Basalts (GB) and Hula Valley (HV). Along the CFZ, we model
198 the major sedimentary basins of Jezreel Valley (JV) and Zevulun Valley (ZV). The coastal plain is underlain by
199 the westward thickening Sedimentary wedge (SW). Geographically, the model extends from the city of Ashdod
200 in the south (31.8° N, 34.6° E) to Hula Valley in the north (33.23° N, 35.72° E) and from the Mediterranean Sea
201 in the west to the Golan Basalts in the east. Figures 4b,c,d illustrate the north-south and east-west cross-sections
202 of the velocity profiles. The numerical domain spans 159 km in the north-south direction and 124 km in the east-
203 west direction. It covers almost 80 % of the Israeli population and a significant part of the population of the
204 Palestinian Authority.
205   Subsurface geometry and the characteristics of the DST trough were obtained from Rosenthal et al., (2019)
206 with modifications for the Hula Valley, obtained from the density log of the Notera 3 (Rybakov et al., 2003). The
207 sedimentary wedge structure retrieved from Gvirtzman et al. (2008) and the Zevulun Valley structure was set
208 using data from Gvirtzman et al. (2011). The basement depth along the model is based on Ben-Avraham et al.,
209 (2002). Five physical quantities describe the viscoelastic material model used in this research: shear wave velocity
210 (Vs), pressure wave velocity (Vp), density (ρ), and seismic quality factors (Qs, Qp) for each point in the
211 computational space. The missing parameters were assessed indirectly by using the correlation presented by
212 Brocher (2008). The main units with their respective velocity, density and quality factors are shown in Table 1.
213   Seismic sources were modeled using the distributed slip model (DSM) developed by Shani-Kadmiel et al.,
214 (2016). DSM is a kinematic model which describes the rupture patch as an elliptic surface with maximum slip at

215   the nucleation point, decaying toward the edges as a pseudo-Gaussian function (Fig. S2). Rupture patch size and

216   displacements were scaled following the relations presented in Wells & Coppersmith (1994). All sources were

217   modeled as left-lateral, vertical strike slips (a dip of 90° and rake of 0°), with a strike of 3° for sources on the

218   DST and a strike of 325° for the CFZ. The moment-rate time function of each point on the rupture patch was set

219   to a GaussianInt pulse (Petersson and Sjogreen, 2017b) with a central frequency of $f_0=0.4$ Hz and a maximum

220   frequency of $f_{max}=1$ Hz.

221   The depth of the model was set to 28 km corresponding to the maximum seismogenic depth in this region

222   (Wetzler and Kurzon, 2016). We assigned a minimum shear wave velocity of 608 m s^{-1} for the uppermost

223   sedimentary layer due to the computational limitations of our system. Grid spacing was set to 76 m in accordance

224   with the minimum shear wave velocity and the maximum frequency of the source. We set the simulation time to

225   120 seconds to allow the slowest waves to propagate across the entire computational domain. The main parameters

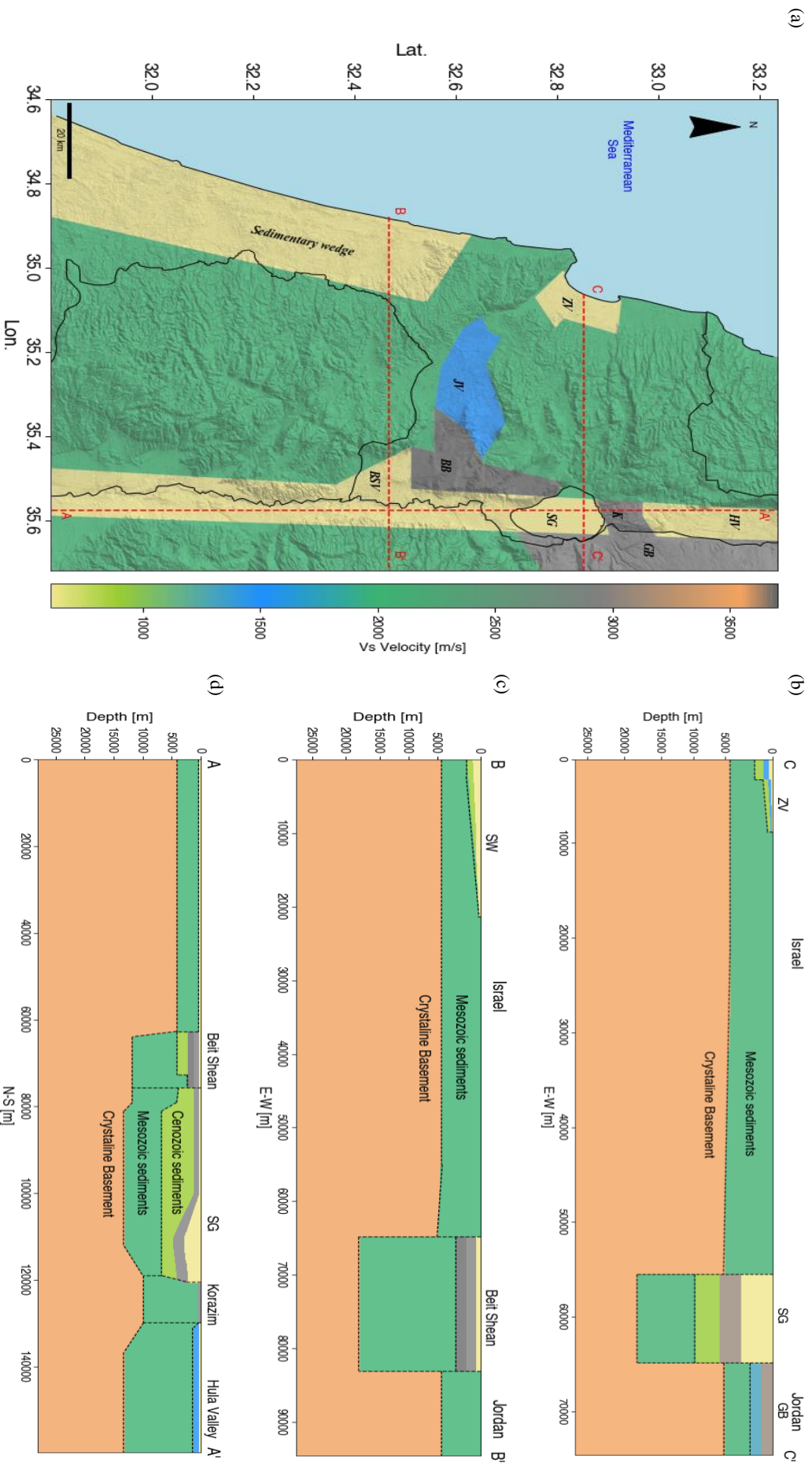226   of the numerical setting are summarized in Table 2.

Figure 4. (a) The numerical model of the computational domain accompanied with subsurface cross-sections, marked with red dashed lines: (b) east-west-cross section through Zevulun Valley, CC' (c) east-west cross-section through the Sedimentary wedge, BB' and (d) north-south cross-section through the DST trough, AA'.

227

9

228   **Table 1.** Material properties of main stratigraphic units used in this work

Model part	Rock Formation	Vs [m s^{-1}]	Vp [m s^{-1}]	Qs	Qp	ρ [Kg m^{-3}]
Regional	Crystalline basement	3550	6000	403	806	2720
	Cenozoic and Mesozoic sediments (Judea/ Talme Yafe, Mount Scopus Avedat, and Lower Saqiye)	2000	3700	160	320	2350
Local variations:						
DST	Cenozoic sediments (Umm Sabune, Bira and Gesher)	887	2380	62	124	2054
	Miocene volcanics (lower basalt)	3698	6330	439.5	879	2790
	Pliocene volcanics (upper basalt)	2947	4900	282	564	2520
	Notera/Lisan	608	2000	39.87	79.74	1900
Hula	Cenozoic sediments	1500	3100	111.5	223	2245
	Notera/Lisan	608	2000	39.87	79.74	1900
JV	Cenozoic sediments (Umm Sabune, Bira, and Gesher)	887	2380	62	124	2054
	Miocene volcanics (lower basalt)	3698	6330	439.5	879	2790
	Cenozoic sediments	1500	3100	111.5	223	2245
ZV	Cenozoic and Senonian sediments (Mount Scopus Avedat and Beit Guvrin)	887	2380	62	124	2054
	Cenozoic sediments (Patish)	1500	3100	111.5	223	2245
	Cenozoic sediments (Kurkar and Yafo)	608	2000	39.87	79.74	1900
SW	Cenozoic sediments (Lower Saqiye)	887	2380	62	124	2054
	Cenozoic sediments (Kurkar and Upper Saqiye)	608	2000	39.87	79.74	1900

229   **Table 2.** Main parameters of the numerical model

Parameters	Value
Model Dimensions (L×W×D)	159.63 Km × 124.45 Km × 28 Km
Spatial spacing (dh)	76 m
Grid size (points)	1.27×10^9
Time step spacing	0.0125 s
Simulated time	120 s
Source Dimensions (L×D)	M 6: 32 Km × 15 Km
	M 7: 38 Km × 22 Km
Source maximum and average slip	M 6: 0.5 and 0.2 m
	M 7: 3 and 1.57 m
Seismic moment (M_0)	M 6: 2.57×10^{18} N·m (Mw 6.21)
	M 7: 2.37×10^{19} N·m (Mw 6.85)
Source fundamental (f_0) and maximal frequencies (f_{max})	0.4 and 1 Hz

230   ### 3.2   Earthquake scenarios and database

231   To examine the variability of ground motions from moderate M 6 and strong M 7 earthquakes, we concentrated

232   on earthquake events nucleating on active segments of the DST system, with known slip deficit, and along the

233 CFZ. We modeled a symmetric bilateral rupture on the Jordan Gorge Fault (JGF-B), Jericho Fault (JF) Carmel

234 Fault Zone (CFZ) and the Shemona Fault (SF), a southward unilateral rupture on the JGF (JGF-U), and a super-

235 shear rupture on the Jordan Valley Fault (JVF) (Fig. 3).

236   The hypocenter for the DST events was placed in the middle of the seismogenic depth; 11 and 13 Km, for

237 the M 6 and M 7 respectively, for the M 6 CFZ, the value was set to 12 Km. The rupture patch was designed to

238 be contained in uniform lithology to prevent super-shear rupture speeds in the shallow parts of our model.

239 Therefore, rupture speed for each scenario was set to 0.9 V_S of the lithology surrounding the nucleation zone. The

240 only exception was the JVF scenario for both M 6 and M 7, in which we modelled super-shear effects. The rupture

241 velocity of each scenario corresponds to the local variations of the sediment's depth. Following the transition of

242 the nucleation zone from the shallow crystalline basement in the south and west parts of the model to the thick

243 Mesozoic and Cenozoic sediments in the north and east, the rupture velocity decreases from 3195 m s^{-1} along

244 the Shemona, Carmel, and Jericho faults to 1800 m s^{-1} along the JGF and JVF faults. As a reference, we simulated

245 a simple two-layered reference model (Ref) on the JGF, with mechanical properties similar to the regional setting,

246 following Aldersons et al., (2003). The scenarios are summarized in Table 3.

247 **Table 3.** Earthquake scenarios

Fault Name	Scenario	Magnitude (M)	Rupture speed (m s^{-1})	Hypocentral depth (Km)
Jordan Gorge	Bilateral rupture (JGF-B)	6, 7	1800	11 and 13
Jordan Gorge	Southward unilateral rupture (JGF-U)	6, 7	1800	11 and 13
Jordan Valley	Bilateral super-shear rupture (JVF)	6, 7	1800	11 and 13
Jericho	Bilateral rupture (JF)	6, 7	3195	11 and 13
Shemona	Bilateral rupture (SF)	7	3195	13
Carmel	Bilateral rupture (CFZ)	6	3195	12
Reference	Bilateral rupture (Ref)	6, 7	3195	11 and 13

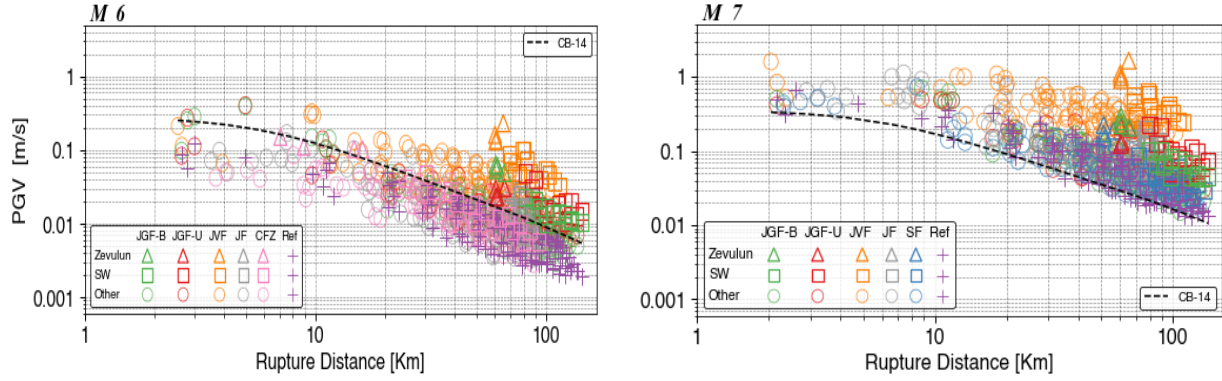## 4   Results

249 In this section, we report the simulation results and the simulation-based attenuation model for M 6 and M 7. We

250 begin with elaborating on the regression process and its deliverable, the attenuation model. Next, we show the

251 correspondence of the model with the simulated database in terms of PGV residuals and examine the contribution

252 of each earthquake scenario to the total deviation. Then, we proceed with looking into single station variability,

253 through maps of the predicted and simulated PGV, with the corresponding residuals at each station. Finally, we

254 examine the PGV and the 5 %- 95 % ground motions significant duration (Ds 595) correspondence between

255 predicted by global GMM's (CB14, Afshari & Stewart, 2016, respectively) and simulated.

4.1   Simulation results

257 For each simulation, we attained a set of 129 synthetic ground motion records (3 components each; N-S, E-W,

258 and vertical) from the network deployed in the computational domain. Next, we calculated the PGV values for

259 each scenario at each station as the maximum value over the three components. We decided to exclude some of

260 the M 7 near-source records (stations: 104,105 and 106 for the JVF scenario and stations: 122,123 and 129 for the

261 JGF-B, JGF-U, and Shemona scenarios) due to high strain values and possible non-linear effects, not compatible

262 with the linearity assumption of our model. In total, our ground motions database consists of 645 and 633 synthetic

263 records for M 6 and M 7, respectively. Figure 5 presents our results in terms of PGV as a function of distance. We

264 use different markers for records from the sedimentary structures of the Zevulun Valley and the Sedimentary

265 wedge to differentiate them from the remaining data.

266 **Figure 4.** Simulation results, PGV-distance space, for bilateral rupture on the Jordan Gorge Fault (JGF-B), Jericho Fault (JF)

267 Carmel Fault Zone (CFZ; for M 6) and the Shemona Fault (SF; for M 7), a southward unilateral rupture on the JGF (JGF-U),

268 and a super-shear rupture on the Jordan Valley Fault (JVF); for M 6 (left) and M 7 (right). The records from Zevulun Valley

269 and the Sedimentary wedge (SW) are marked with triangles and rectangles, respectively. The other records are marked with

270 circles; the reference records are marked with pluses. For comparison, the CB-14 is plotted for a strike-slip fault, $Z_{2.5}$=0.42

271 Km and V_{S30} =1686 m/s (representing averaged values over all the sites).

272 ### 4.2 Statistical analysis of ground motions results

273 The next step was to formulate a parametric ground motion attenuation model (AM) for the two magnitudes based

274 on our simulations. Such a model will provide an estimate for the median ground motions and their variability.

275 The general parametric form of the AM for both M 6 and M 7 is presented in Eq. (1):

276 $$\ln Y = a \ln\left(\sqrt{R_{RUP}^2 + b}\right) + c \ln \left(\frac{V_{s,surf}}{V_{s,ref}}\right) + d\, Z_2 + e \,\pm\, \sigma \tag{1}$$

277 Where Y is ground motion parameter. Due to the bandwidth of our numerical models (0.1 to 1 Hz), we formulated

278 the AM in terms of PGV. We use the closest distance to the fault rupture plane (R_{RUP} as defined in CB14) as the

279 initial explanatory variable. To improve the accuracy of the model, we incorporated two additional variables into

280 the regressions: surface shear wave velocity at the site ($V_{S,\,surf}$) and the depth to $V_S = 2$ km s^{-1} (Z_2), which is the

281 depth to the hard Mesozoic sediments (top Judea Gr.) considered the primary reflector in the region. *a, b, c, d*, and

282 *e* are model coefficients, and σ is the standard deviation. The $V_{S,\,ref}$ is the shear wave velocity corresponding to

283 the Judea Gr. in the computational domain, which in our model equals 2000 m s^{-1}.

284 The process of minimizing the residuals as a function of each explanatory variable can be found in the

285 supplementary material (Fig. S3). We used $V_{S,\,surf}$ instead of the more common V_{S30}, as our grid resolution is 76

286 m, preventing us from accurately determining the time-averaged shear wave velocity in the top 30 m of each site

287 in our model. The coefficients and the total standard deviation for each model are summarized in Table 4.

Table 4. Regression coefficients for the attenuation model (AM)

Mag.	IM	a	b	c	d		e		Standard Deviation (σ)
					R_{rup} >58 km and z_2 >0	R_{rup} <58 km or z_2=0	R_{rup} >58 km and z_2 >0	R_{rup} <58 km or z_2=0	
6	PGV	-1.01	59.34	-0.685	0		0.56		0.6
7	PGV	-1.22	151.81	-0.669	0.56	0	2.08	2.42	0.629

4.3   AM Variability

We then examined the simulated data and the contribution of each scenario to the AM variability. We calculated the within-event (δW) and between-event (δB) residuals (see Al Atik et al., (2010)) for each magnitude and distance:

$$\delta W_{i,j} = \ln PGV_{i,j}^{\ sim} - \ln PGV_i^{\ m} \tag{2}$$

$$\delta B_i = \ln PGV_i^{\ m} - \ln PGV^{\ AM} \tag{3}$$

where $PGV_{i,j}^{\ sim}$ is the simulation value for event i and recording j, PGV_i^m is the median for event i, and PGV^{AM} is the AM median value. The total residual is the sum of the within and between event residuals.

The residuals are presented in Fig. 6: total (Fig. 6a and 6b), within-event (Fig. 6c and 6d), and between-events (Fig. 6e and 6f). The total residuals (Fig. 6a and 6b) show a large underprediction of the PGV from the JVF scenario (orange) on which we modeled a super-shear rupture, up to a ratio of 2.5 and 2 in the Zevulun Valley (orange triangles), for M 6 and M 7, respectively. However, the AM also exhibits over predictions; The PGV from the scenarios nucleated in the crystalline basement (SF, JF, and CFZ), with rupture speed= 3195 m s^{-1}), are overpredicted down to a ratio of more than -1 (in ln units).

Some within-event residuals exhibit distance dependency; for M 7, the JVF (super-shear model) and JGF-U (directivity model) residuals increase with rupture distances greater than 20 km. The JVF residuals also demonstrate the same distance dependency for M 6; however, the effect is less prominent when compared to M7.

The effect of the rupture directivity (JGF-U) is demonstrated in comparing the Zevulun Valley and the Sedimentary wedge within-event residuals (Fig. 6c and 6d). While in a symmetric rupture (JGF-B), the seismic energy dissipates equally into the north and south parts of the model, in an asymmetric rupture (JGF-U), more energy propagates toward the south, resulting in stronger ground motions at the Sedimentary wedge (Fig. 5). However, the ground motions are less intensive at the Zevulun Valley compared to the symmetric rupture. As a result, the within-event residuals for Zevulun Valley are higher for the JGF-B scenario compared to the JGF-U scenario, while for the Sedimentary wedge, the opposite is true. Most clearly, the JVF between-event residuals are the highest for both M 6 and M 7 with a ratio of 1 (Fig. 6e, and 6f).
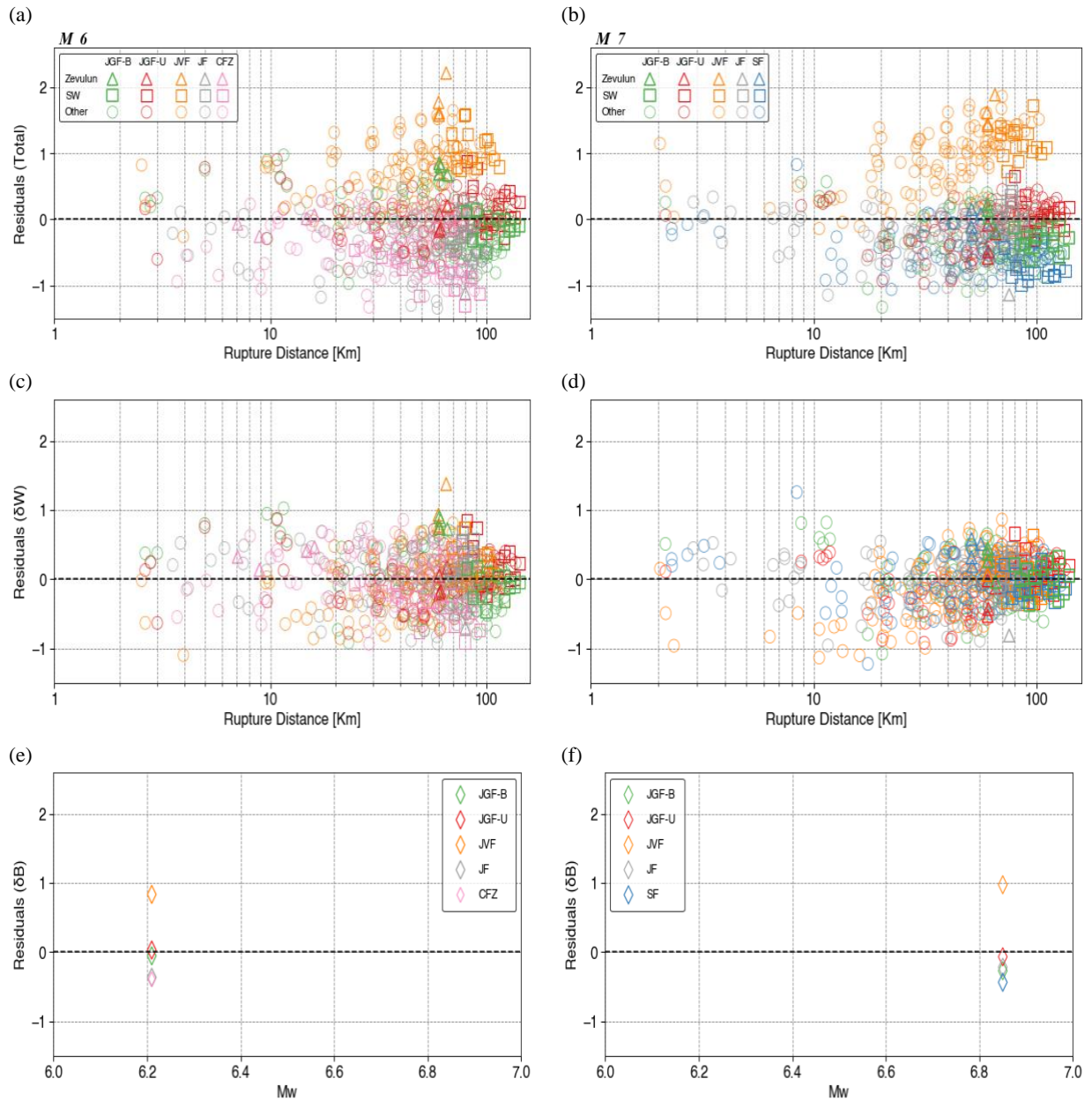
Figure 5. Residuals between simulated and attenuation model (AM) PGV as a function of rupture distance (R_{RUP}), for bilateral rupture on the Jordan Gorge Fault (JGF-B), Jericho Fault (JF) Carmel Fault Zone (CFZ; for M 6) and the Shemona Fault (SF; for M 7), a southward unilateral rupture on the JGF (JGF-U), and a super-shear rupture on the Jordan Valley Fault (JVF); for M 6 (left) and M 7 (right); (a) and (b) total residuals, (c) and (d) within-event (δW) residuals, (e) and (f) between-event (δB) residuals. The records from Zevulun Valley and the Sedimentary wedge (SW) are marked with triangles and rectangles, respectively. The other records are marked with circles. Residuals are in ln units.

We further study the single station variation of ground motions and quantify the misfit between the simulated PGV and the AM PGV. We calculate the mean ground motion and its standard deviation at each station. The residuals for single station k were calculated as follows:

$$\delta_k = \ln PGV_k^{sim} - \ln PGV_k^{AM} \tag{4}$$

14

324 where PGV_k^{sim} and PGV_k^{AM} are the simulated and predicted mean PGV at station k, respectively. Figure 7 and

325 Figure 8 show the mean simulated and mean AM PGVs for M 6 and M 7, respectively. For each station, we also

326 plot the standard deviation using a scaled diameter circle.

327   Both figures show that simulated ground motions variability at a single station is large, not fully covered

328 by the AM. For example, simulated ground motions at station 129 located on the Hula Valley exhibit a significant

329 standard deviation. For M 6, it is the largest value (green triangle) of 0.17 m s^{-1} compared to 0.09 m s^{-1} (indigo)

330 predicted by the AM, while for M 7, the largest standard deviation is 0.59 m s^{-1} (orange triangle) compared to

331 0.02 m s^{-1} (light green triangle) observed at station 127 located on the Zevulun Valley As a result, there is a large

332 discrepancy between the simulated and AM values at specific stations.

333   In general, higher mean PGV values are accompanied by a larger standard deviation for both magnitudes;

334 however, the ground motions variability is larger for M 7.

335 **4.4 Comparison with global models**

336 To examine the agreement between our simulations with an instrumental, global GMM, we calculated the total

337 residuals between PGVs from our simulations and PGVs predicted by the CB 14 model. The CB-14 PGVs were

338 calculated for a strike-slip fault, where we used the surface shear wave velocity as the V_{s30} parameter and the basin

339 response term Z_2 as $Z_{2.5}$. Figure 9 shows the total residuals for the AM and CB14 models as a function of distance

340 (R_{RUP}). For both magnitudes, the AM (mean and standard deviation) oscillates near the zero-model bias (black

341 horizontal dotted line). However, it deviates when approaching the region containing rupture distances typical of

342 the Zevulun Valley. The effect is more noticeable for M 7. Figure 9 also shows that the CB14 is less consistent

343 and performs differently for each magnitude. While for M 6, the GMM mostly over predicts (negative values) the

344 simulated PGV (until reaching ZV and SW rupture distances zones), for M 7, it mostly under predicts them

345 (positive values), except for large distances, up to a factor of 2 and above. In addition, the residuals calculated

346 with respect to CB-14 exhibit a significant standard deviation of the mean ground motion, with considerably larger

347 variability for M 7.

348   It is important to note that, by averaging the PGVs, we subdue the performance of both models at individual

349 stations/Rupture distances; thus, we cannot analyze the residual's spatial variations at a specific location.

350 However, it is sufficient to demonstrate that the global model deviates considerably from simulated ground

351 motions.
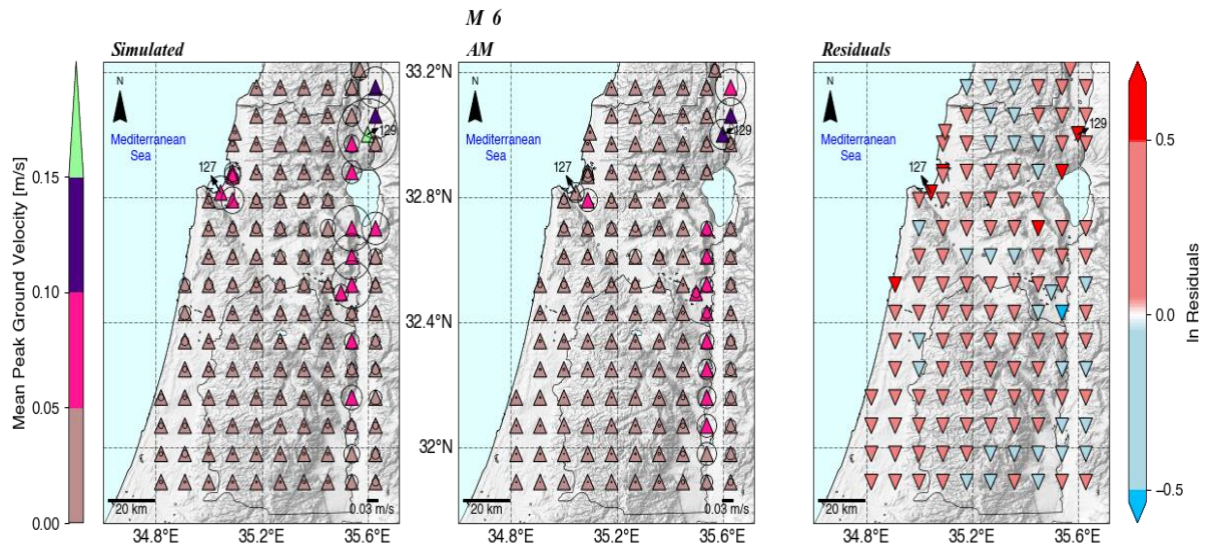
Figure 6. Map view of simulated and AM mean PGV (triangles) for M 6 and their standard deviation (diameter of the circles) at each station, with the respective residuals in ln units (inverted triangles).

Figure 7. Map view of simulated and AM mean PGV (triangles) for M 7 and their standard deviation (diameters of the circles) at each station, with the respective residuals in ln units (inverted triangles).
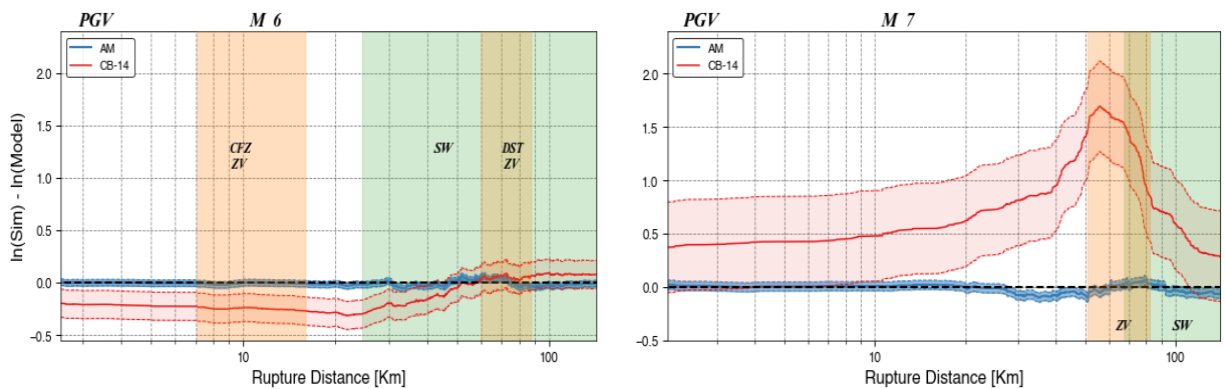

Figure 8. PGV Residuals between simulated (Sim) and predicted by the AM (blue) and CB-14 (red) models, as a function of rupture distance (R_{RUP}), for M 6 (left) and M 7 (right). Thick lines represent the mean, and the shaded region denotes the

standard deviation at each distance. The green and yellow shaded regions indicate the range of rupture distances related to the Sedimentary wedge (SW) and the Zevulun Valley (ZV), respectively. Residuals are in ln units.

4.5 Significant duration

Another important intensity measure is the significant duration (Ds595), the time interval between 5 % to 95 % of the cumulative seismic energy (Arias Intensity) at a site. Figure 10 shows the simulated and empirical Ds 595 values as a function of rupture distance. The typical increase of the empirical model with distance is captured in the reference (laterally homogenous) model. However, for all other models, the significant duration remains nearly constant, at ruptures distances larger than 20 km. In addition, the empirical GMM mostly under-predicts the simulated values between 2 to 50 Km for both magnitudes.

We postulate that this is caused by the complex geological setting of our model. The impact of geological complexity is reflected in Ds 595 values from near-source stations, Zevulun Valley (triangles), and the Sedimentary wedge (rectangles). At near-source stations, the significant duration is large due to the effects of deep sedimentary structures along the DST, which also prolongs the path duration of the ground motions in other sites (Shimony et al., 2021). On the contrary at the Zevulun Valley and the SW, the energy accumulates faster than in other sites, as the ground motions are amplified, reaching 95 % of the total energy over a shorter duration. Interestingly, the significant duration in Zevulun Valley is lower than in the Sedimentary wedge. As we expect from deep sedimentary structures to prolong shaking duration, it may sound counterintuitive. However, it is explained by the relative proximity of the Zevulun Valley to the rupture. Whereas in Zevulun Valley, most of the energy arrives as a pulse at the beginning of the record, the energy at the more distant Sedimentary wedge accumulates more gradually and reaches its maximum almost at the end of the record, resulting in longer Ds595 values. In general, there is no large deviation between the simulated significant duration for M 6 and M 7. However, the empirical model shows a longer duration for M 7. This resembles in source duration is related to the DSM settings, more specifically to the source fundamental frequency, which in our study, is the same for both magnitudes; and it is a subject for testing in future works.
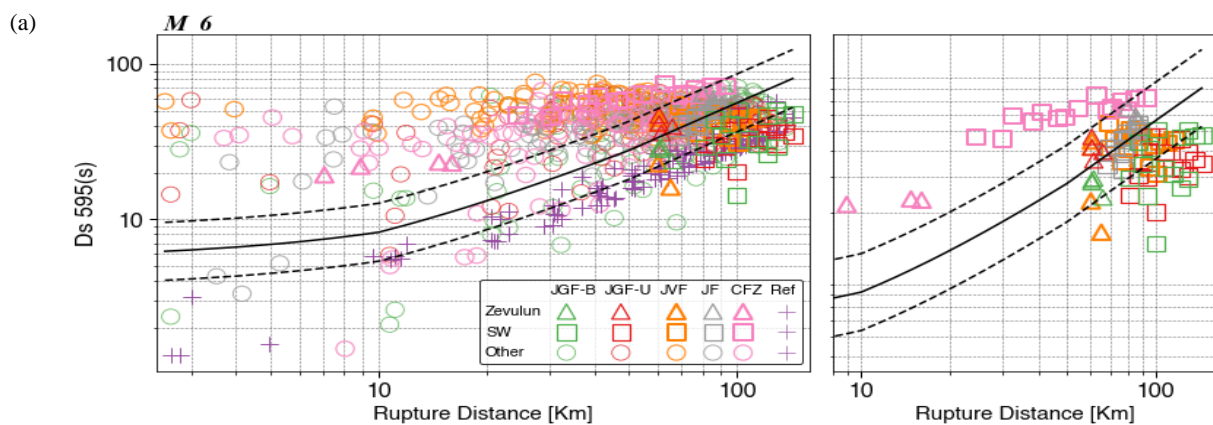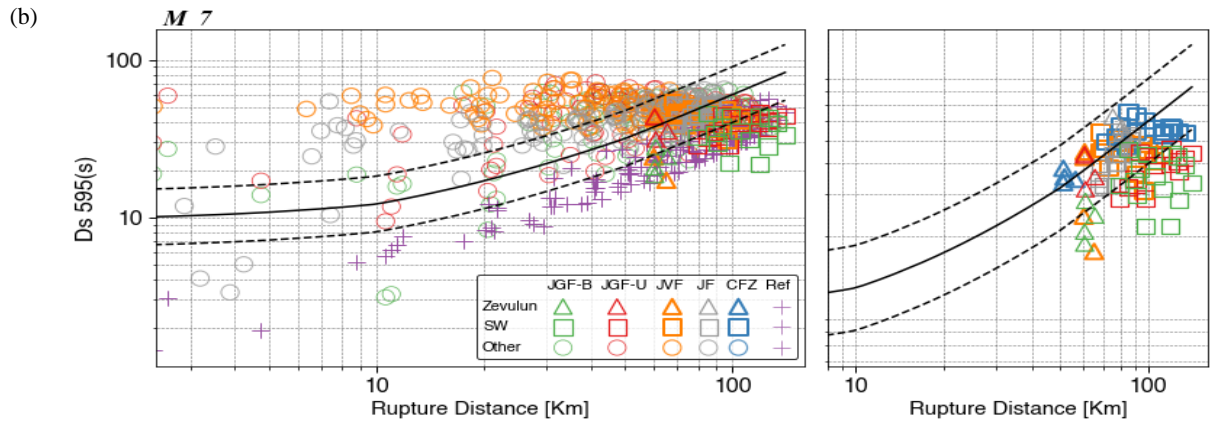
Figure 9. Comparison of 5 % to 95 % ground motions significant duration (Ds 595) between simulated and empirical GMM (Afshari and Stewart, 2016), for bilateral rupture on the Jordan Gorge Fault (JGF-B), Jericho Fault (JF) Carmel Fault Zone (CFZ; for M 6) and the Shemona Fault (SF; for M 7), a southward unilateral rupture on the JGF (JGF-U), and a super-shear rupture on the Jordan Valley Fault (JVF); for M 6 (a) and M 7 (b). Main plots (left) accompanied with subplots showing only the records from the Zevulun Valley and the Sedimentary wedge (right). Solid and dashed lines represent the median and the standard deviation of the empirical GMM, respectively. The records from Zevulun Valley and the Sedimentary wedge (SW) are marked with triangles and rectangles, respectively. The other records are marked with circles.

5   Discussion and Summary

A strong earthquake in Israel is imminent. However, up to date, a comprehensive regional GMM describing the spatial variability of ground motions has not yet been developed. This is mainly due to low seismicity rates and magnitude bounded strong motion database, coupled with sparse instrumental coverage. The current ground motion database lacks events with magnitude M > 6. To fill this gap and examine different source and path effects on ground motions variability, we simulated M 6 and M 7 earthquakes with different source and path properties. Subsequently, to study the ground motions variability, we developed a parametric attenuation model (AM) of PGV for M 6 and M 7 earthquakes, based on R_{RUP}, Z_2, and $V_{S, surf}$ explanatory values.

Our analysis shows that the AM was unable to fully capture the variability of the simulated ground motions. Except for the Jordan Valley Fault (JVF) scenarios, the AM overestimates most of the modeled ground motions. We postulate that this overestimation results from the outlier, higher PGV values from the JVF scenario (Fig. 5), shifting the average ground motion toward them. Also, the within-event residuals for the JVF scenario show a distance dependency for $R_{RUP} > 20$ Km, continuing to grow away from the fault. We describe this scenario as a "black swan" of our simulations and account its outlier behavior to the effects of the super-shear rupture, specific to this model, affecting both the source and path terms of the ground motions (Fig.6). Super-shear ruptures behave differently from sub-shear ruptures in many aspects. Most pertinent to our analysis is the slow energy decay of the super-shears relative to sub-shears (Bhat et al., 2007); thus, it cannot be fully captured by our AM, which is based mainly on sub-shear ruptures. In addition, it was found that Z_2, depth to Mesozoic rock, has a very small impact (<0.001) on the standard deviation for the M 6, reducing it from 0.5998 to 0.5988 (Fig. S3). As a result, the M 6 model depends only on rupture distance and $V_{S, surf}$. For M 7, Z_2 is a good predictor for soil sites ($Z_2 > 0$) located >58 Km from the source, including the Zevulun Valley and the Sedimentary wedge (Fig. 6d), imposing a great seismic hazard. We do not see a clear dependence of the deep sedimentary structures with Z_2, along the DST. We speculate that Their site response may be masked by nearby source effects and requires additional analysis.

For each scenario, both magnitudes considered, we observed high PGV values at the Zevulun Valley and the Sedimentary wedge associated with local site effects. These sedimentary structures exhibit a larger discrepancy between the simulated and AM PGV values when compared with other sites. Such deviation indicates that the AM does not fully capture the site effects of these complex structures, and future model refinements are required. Likewise, the single station variability shows that the simulated values' highest mean and standard deviation were in Zevulun Valley and near-source stations. In addition, a relatively high standard deviation was also found in the Sedimentary wedge for M 7. This large single station variability is, apparently, the impact of the outlier JVF PGV values. The AM does not account for the standard deviation at near-source and Zevulun Valley stations for the M 6 and almost at all stations for the M 7. In fact, as the AM was unable to capture the simulated JVF PGV values, it is expected that the single station variability cannot be captured either. Furthermore, we show that the larger discrepancy for M 7 is due to the larger deviation of the JVFs ground motions from the mean (Fig. 6d,e).

Noteworthy to mention is that while the effect of the super-shear rupture on the AM performance is systematic over the entire computational domain, the effect of the southward directivity is distance-dependent, path effect, increasing towards the south, related to a larger amount of energy discharged in this direction. Additional records of super-shear and directivity ruptures and accounting for these source effects by additional model terms will improve the performance of the AM and will assist in better understanding the implications of these phenomena on the seismic hazard in Israel.

The comparison of the simulated ground motions with a global GMM (CB-14) showed that this model is not well constrained for the simulated ground motions and does not capture their total variability. We note that the comparison was performed on a single IM, the PGV values, one of several intensity measures provided by the CB-14. Thus, our findings are pertinent to the variability of PGV solely. It should be noted that PGV is a good proxy for structural damage (e.g., to Kaestli & Fäh, (2006); Wald et al., (1999)), hence a crucial parameter for seismic hazard mitigation. This discrepancy between modeled PGV and CB-14 PGVs will inevitably result in a discrepancy in the evaluation of structural damage.

The significant duration (DS595) comparison showed again that the imported model performs differently than the simulated ground motion and cannot explain the local variability due to complex geological structure, affecting the source, path and site terms of the ground motions. However, we note that the Ds595 from our simulations were calculated based on low frequency content (<1Hz) and may be biased from Ds595 calculated based on the complete spectrum comprised of both low and high frequencies. The effects of the frequency content on significant duration may be a potential topic for research in future works.

We acknowledge that our AM is not independent of the evaluated models, thus describing both their explanatory and predictive power (Mak et al., 2017). However, our goal was not to develop an independent and comprehensive GMM but to study the ground motion variability through a parametric model.

Recently, Maiti et al., (2021) developed a suite of nine GMMs for Israel, in the magnitude range of 3 to 8 and distance range of 1 to 300 Km. These models are formulated in Fourier amplitude spectra (FAS) and are based on one empirical and four simulated ground motion datasets and two empirical host models. The simulated ground motions were generated using the Stochastic Method SIMulation (SMSIM) model of Boore (2003), with a unique set of parameters for each simulation, calibrated with the empirical ground motions dataset (discussed in detail in Yagoda-Biran et al., (2021)). However, the GMMs do not fully account for a local source, path, and site effects

due to sparse empirical database at large magnitudes (M > 6) and the utilization of a point-source stochastic simulation method. This method is useful for simulating mean ground motions. Yet, it is less appropriate for simulating site-specific and earthquake-specific ground motions and low-frequency ground motions, which are affected by the 3D geometry of the computational domain. The AM presented in this work is based on 3D simulations and incorporates a finite fault source with different rupture properties. This is the first step toward developing a regional GMM, accounting for local source, path, and site effects. In subsequent work, which is beyond the scope of the current research, we intend to develop a complete GMM for Israel, which will include all the magnitudes and will be based on empirical (M < 6) as well as on synthetic (M > 6) databases. In addition, we plan to incorporate new path and site terms such as $Z_{0.8}$ for the Zevulun valley and the Sedimentary wedge, distance-dependent and rupture velocity-dependent attenuation for Directivity and super-shear ruptures, among others; as well as a source term for super-shear ruptures. Such a model is expected to perform better than imported global models by maintaining both; a lower aleatory variability and, as new synthetic data will be added to the database, reduced epistemic uncertainty of the median ground motions (Abrahamson et al., 2019).

The population of Israel is fast-growing, with an annual rate of 1.8 % (OECD 2020 data), compared with the 0.4 % average of the OECD. Coupled with fast economic growth of 4.5 % (OECD 2019 data), the demand for housing and infrastructure constantly elevates the seismic risk in Israel. Our work shows that the ground motions in Israel from M 6 and M 7 earthquakes are expected to be very damaging, up to 8-9 EMS (Fig. S4). Furthermore, the modeled ground motions exhibit considerable spatial variability, which imported GMMs do not fully capture. The development of a local comprehensive GMM model is therefore critical for the mitigation of seismic risk. In the foreseen future, the moderate-strong ground motion data gap will be filled by synthetic ground motion records from systematic numerical simulations.

Data and resources

Israel Seismic catalog (Fig. 1a), expanded after Wetzler & Kurzon (2016) catalog and the configuration of the Israel seismic network (Fig. 1b) after Kurzon et al., (2020) can be found at https://earthquake.co.il/en/earthquake/searchEQS.php and https://earthquake.co.il/en/network/accNetwork.php, respectively. The ground motions database of Israel (Fig. 2) discussed in Yagoda-Biran et al., (2021) is available at https://earthquake.co.il/en/hazards/EngSeismology.php. The Taub Center population projections for Israel are accessible at https://www.taubcenter.org.il/en/pr/population-projections-for-israel-2017-2040/. OECD population and economic growth rates can be found at https://data.oecd.org/israel.htm#profile-economy. Simulations were performed using SW4 version 2.0 (v2.0; Petersson and Sjögreen, 2017a), an open-source package for wave propagation simulations, available at github.com/geodynamics/sw4 (last accessed June 2021). Data processing was done with the pySW4 package from Shahar Shani-Kadmiel, available at https://github.com/shaharkadmiel/pySW4 (last accessed July 2021), and "obspy" (Beyreuther et al., 2010), developed for numerical seismology. Figures were prepared with Matplotlib (Hunter, 2007) and Cartopy (Met Office, 2016). Peak ground velocity (PGV) values, according to Campbell and Bozorgnia (2014), were calculated using the Next Generation Attenuation-West Project (NGA-West2) ground-motion prediction equations (GMPEs) excel file, available at https://apps.peer.berkeley.edu/ngawest2/databases/ (last accessed July 2021). The supplemental material includes: (1) synthetic station network deployed in our models (Fig. S1); (2) distributed slip model (DSM) slip distribution and rupture time (Fig. S2); (3) the evolution of the residuals between simulated

491 and attenuation model (AM) PGV for M 6 and M 7 (Fig. S3) and (4) map view of simulated mean EMS intensity

492 calculated according to Kaestli & Fäh, (2006).

493 *Competing interests*. The authors declare that they have no conflict of interest.

497 **References**

498 Abrahamson, N. A., Kuehn, N. M., Walling, M., and Landwehr, N.: Probabilistic seismic hazard analysis in

499 california using nonergodic ground-motion models, Bull. Seismol. Soc. Am., 109, 1235–1249,

500 https://doi.org/10.1785/0120190030, 2019.

501 Afshari, K. and Stewart, J. P.: Physically parameterized prediction equations for significant duration in active

502 crustal regions, Earthq. Spectra, 32, 2057–2081, https://doi.org/10.1193/063015EQS106M, 2016.

503 Agnon, A.: Pre-instrumental earthquakes along the Dead Sea rift, in: Modern Approaches in Solid Earth

504 Sciences, vol. 6, Springer, 207–261, https://doi.org/10.1007/978-94-017-8872-4_8, 2014.

505 Aldersons, F., Ben-Avraham, Z., Hofstetter, A., Kissling, E., and Al-Yazjeen, T.: Lower-crustal strength under

506 the Dead Sea basin from local earthquake data and rheological modeling, Earth Planet. Sci. Lett., 214, 129–142,

507 https://doi.org/10.1016/S0012-821X(03)00381-9, 2003.

508 Ambraseys, N. N.: Comparison of frequency of occurrence of earthquakes with slip rates from long-term

509 seismicity data: The cases of Gulf of Corinth, Sea of Marmara and Dead Sea Fault Zone, Geophys. J. Int., 165,

510 516–526, https://doi.org/10.1111/j.1365-246X.2006.02858.x, 2006.

511 Anderson, J. G. and Brune, J. N.: Probabilistic seismic hazard analysis without the ergodic assumption, Seismol.

512 Res. Lett., 70, 19–28, https://doi.org/10.1785/gssrl.70.1.19, 1999.

513 Al Atik, L., Abrahamson, N., Bommer, J. J., Scherbaum, F., Cotton, F., and Kuehn, N.: The variability of

514 ground-motion prediction models and its components, Seismol. Res. Lett., 81, 794–801,

515 https://doi.org/10.1785/gssrl.81.5.794, 2010.

516 Bartov, Y., Steinitz, G., Eyal, M., and Eyal, Y.: Sinistral movement along the Gulf of Aqaba - Its age and

517 relation to the opening of the Red Sea, Nature, 285, 220–222, https://doi.org/10.1038/285220a0, 1980.

518 Ben-Avraham, Z., Ginzburg, A., Makris, J., and Eppelbaum, L.: Crustal structure of the Levant Basin, eastern

519 Mediterranean, 346, 23–43, https://doi.org/10.1016/S0040-1951(01)00226-8, 2002.

520 Beyreuther, M., Barsch, R., Krischer, L., Megies, T., Behr, Y., and Wassermann, J.: ObsPy: A python toolbox

521 for seismology, Seismol. Res. Lett., 81, 530–533, https://doi.org/10.1785/gssrl.81.3.530, 2010.

522 Bhat, H. S., Dmowska, R., King, G. C. P., Klinger, Y., and Rice, J. R.: Off-fault damage patterns due to

523 supershear ruptures with application to the 2001 Mw 8.1 Kokoxili (Kunlun) Tibet earthquake, J. Geophys. Res.

524 Solid Earth, 112, 1–19, https://doi.org/10.1029/2006JB004425, 2007.

525 Boore, D. M.: Simulation of ground motion using the stochastic method, Pure Appl. Geophys., 160, 635–676,

526 https://doi.org/10.1007/PL00012553, 2003.

527 Brocher, T. M.: Key elements of regional seismic velocity models for long period ground motion simulations, J.

528   Seismol., 12, 217–221, https://doi.org/10.1007/s10950-007-9061-3, 2008.

529   Campbell, K. W. and Bozorgnia, Y.: NGA ground motion model for the geometric mean horizontal component

530   of PGA, PGV, PGD and 5% damped linear elastic response spectra for periods ranging from 0.01 to 10 s,

531   Earthq. Spectra, 24, 139–171, https://doi.org/10.1193/1.2857546, 2008.

532   Campbell, K. W. and Bozorgnia, Y.: NGA-West2 ground motion model for the average horizontal components

533   of PGA, PGV, and 5% damped linear acceleration response spectra, Earthq. Spectra, 30, 1087–1114,

534   https://doi.org/10.1193/062913EQS175M, 2014.

535   Chaljub, E., Moczo, P., Tsuno, S., Bard, P. Y., Kristek, J., Käser, M., Stupazzini, M., and Kristekova, M.:

536   Quantitative comparison of four numerical predictions of 3D ground motion in the Grenoble Valley, France,

537   Bull. Seismol. Soc. Am., 100, 1427–1455, https://doi.org/10.1785/0120090052, 2010.

538   Douglas, J. and Aochi, H.: A survey of techniques for predicting earthquake ground motions for engineering

539   purposes, Surv. Geophys., 29, 187–220, https://doi.org/10.1007/s10712-008-9046-y, 2008.

540   Garfunkel, Z.: Lateral motion and deformation along the Dead Sea transform, in: Modern Approaches in Solid

541   Earth Sciences, vol. 6, Springer International Publishing, 109–150, https://doi.org/10.1007/978-94-017-8872-

542   4_5, 2014.

543   Graves, R. and Pitarka, A.: Refinements to the Graves and Pitarka (2010) broadband ground-motion simulation

544   method, Seismol. Res. Lett., 86, 75–80, https://doi.org/10.1785/0220140101, 2015.

545   Graves, R., Jordan, T. H., Callaghan, S., Deelman, E., Field, E., Juve, G., Kesselman, C., Maechling, P., Mehta,

546   G., Milner, K., Okaya, D., Small, P., and Vahi, K.: CyberShake: A Physics-Based Seismic Hazard Model for

547   Southern California, Pure Appl. Geophys., 168, 367–381, https://doi.org/10.1007/s00024-010-0161-6, 2011.

548   Grünthal, G., Hakimhashemi, A., Schelle, H., Bosse, C., and Wahlström, R.: The long-term temporal behaviour

549   of the seismicity of the Dead Sea Fault Zone and its implication for time-dependent seismic hazard assessments,

550   https://doi.org/10.2312/GFZ.b103-09098, 2009.

551   Gvirtzman, Z., Zilberman, E., and Folkman, Y.: Reactivation of the Levant passive margin during the late

552   Tertiary and formation of the Jaffa Basin offshore central Israel, J. Geol. Soc. London., 165, 563–578,

553   https://doi.org/10.1144/0016-76492006-200, 2008.

554   Gvirtzman Z., I. M. and Sagee, Y.: Re-processing and geological re-interpretation of old seismic lines of Haifa

555   bay, Geol. Surv. Isr. GSI/27/2011, 2011.

556   Gvitzman, Z. and Zaslavsky, Y.: Map of Zones with Potentially High Ground Motion Amplification:

557   Explanatory Notes, Rep. Num. GSI/15/2009, 2009.

558   Hamiel, Y., Piatibratova, O., and Mizrahi, Y.: Creep along the northern Jordan Valley section of the Dead Sea

559   Fault, Geophys. Res. Lett., 43, 2494–2501, https://doi.org/10.1002/2016GL067913, 2016.

560   Hunter, J. D.: Matplotlib: A 2D graphics environment, Comput. Sci. Eng., 9, 90–95,

561   https://doi.org/10.1109/MCSE.2007.55, 2007.

562   Israel Standards Institution: Standard SI 413. Design Provisions for Earthquake Resistance of Structures.

563   Amendment No. 5, 2013.

564   Kaestli, P. and Fäh, D.: Rapid estimation of macroseismic effects and Shakemaps using macroseismic data, in:

565   1st European Conf. Earthquake Engineering and Seismology, 1535, 2006.

566   Kuehn, N. M., Abrahamson, N. A., and Walling, M. A.: Incorporating nonergodic path effects into the NGA-

567   west2 ground-motion prediction equations, Bull. Seismol. Soc. Am., 109, 575–585,

https://doi.org/10.1785/0120180260, 2019.

Kurzon, I., Nof, R. N., Laporte, M., Lutzky, H., Polozov, A., Zakosky, D., Shulman, H., Goldenberg, A., Tatham, B., and Hamiel, Y.: The "TRUAA" seismic network: Upgrading the Israel Seismic Network-toward national earthquake early warning system, Seismol. Res. Lett., 91, 3236–3255, https://doi.org/10.1785/0220200169, 2020.

Lan, X., Xing, H., Zhou, J., and Zhao, J. X.: A comparison of the source, path, and site effects of the strong-motion records from the western and the southwestern parts of China with modern ground-motion prediction equations, Bull. Seismol. Soc. Am., 109, 2691–2709, https://doi.org/10.1785/0120180293, 2019.

Maiti, S. K., Yagoda-Biran, G., and Kamai, R.: A Suite of Alternative Ground-Motion Models (GMMs) for Israel, Bull. Seismol. Soc. Am., 111, 2177–2194, https://doi.org/10.1785/0120210003, 2021.

Mak, S., Cotton, F., and Schorlemmer, D.: Measuring the performance of ground-motion models: The importance of being independent, https://doi.org/10.1785/0220170097, 2017.

Met Office: Cartopy: a cartographic python library with a matplotlib interface, http://scitools.org.uk/cartopy, 2016.

Mizutori, M. and D'ebarati, G.: The human cost of disasters: an overview of the last 20 years (2000-2019), UN Off. Disaster Risk Reduction., https://doi.org/10.18356/79b92774-en, 2020.

Pesaresi, M., Ehrlich, D., Kemper, T., Siragusa, A., Florczyk, A., Freire, S., and Corbane, C.: Atlas of the Human Planet 2017. Global Exposure to Natural Hazards. EUR 28556 EN, 92 pp., 2017.

Petersson, N. A. and Sjogreen, B.: SW4 Users Guide, Lawrence Livermore Natl. Lab. Tech. Rep. LLNL-SM, 662014, 2014.

Petersson, N. A. and Sjogreen, B.: SW4, version 2.0, Computational Infrastructure of Geodynamics, https://doi.org/10.5281/zenodo.1045297, 2017a.

Petersson, N. A. and Sjogreen, B.: User's guide to SW4, version 2.0,LLNL-SM-741439., https://doi.org/., 2017b.

Pitarka, A., Akinci, A., De Gori, P., and Buttinelli, M.: Deterministic 3D Ground-Motion Simulations (0–5 Hz) and Surface Topography Effects of the 30 October 2016 Mw 6.5 Norcia, Italy, Earthquake, Bull. Seismol. Soc. Am., https://doi.org/10.1785/0120210133, 2021.

Rosenthal, M., Ben-Avraham, Z., and Schattner, U.: Almost a sharp cut – A case study of the cross point between a continental transform and a rift, based on 3D gravity modeling, 761, 46–64, https://doi.org/10.1016/j.tecto.2019.04.012, 2019.

Rybakov, M., Fleischer, L., and ten Brink, U.: The Hula Valley subsurface structure inferred from gravity data, Isr. J. Earth Sci., 52, 113–122, https://doi.org/10.1560/WF6V-4BVG-GXQM-PKVR, 2003.

Sadeh, M., Hamiel, Y., Ziv, A., Bock, Y., Fang, P., and Wdowinski, S.: Crustal deformation along the Dead Sea Transform and the Carmel Fault inferred from 12 years of GPS measurements, J. Geophys. Res. Solid Earth, 117, https://doi.org/10.1029/2012JB009241, 2012.

Shamir, G., Bartov, Y., Sneh, A., Fleisher, L., Arad, V., and Rosensaft, M.: Preliminary seismic zonation in Israel, earthquake.co.il28 , pp., 2001.

Shani-Kadmie, S., Tsesarsky, M., and Gvirtzman, Z.: Distributed slip model for forward modeling strong Earthquakes, Bull. Seismol. Soc. Am., 106, 93–103, https://doi.org/10.1785/0120150102, 2016.

Shani-Kadmiel, S., Volk, O., Gvirtzman, Z., and Tsesarsky, M.: Ground motion amplification atop the complex

sedimentary basin of Haifa Bay (Israel), Bull. Earthq. Eng., 18, 821–836, https://doi.org/10.1007/s10518-018-00533-9, 2020.

Shi, Z. and Ben-Zion, Y.: Dynamic rupture on a bimaterial interface governed by slip-weakening friction, Geophys. J. Int., 165, 469–484, https://doi.org/10.1111/j.1365-246X.2006.02853.x, 2006.

Shimony, R., Gvirtzman, Z., and Tsesarsky, M.: Seismic energy release from intra-basin sources along the dead sea transform and its influence on regional ground motions, Bull. Seismol. Soc. Am., 111, 295–308, https://doi.org/10.1785/0120200215, 2021.

Wald, D. J., Quitoriano, V., Heaton, T. H., and Kanamori, H.: Relationships between peak ground acceleration, peak ground velocity, and modified mercalli intensity in California, Earthq. Spectra, 15, 557–564, https://doi.org/10.1193/1.1586058, 1999.

Walling, M. . and Abrahamson, N. .: Non-Ergodic Probabilistic Seismic Hazard Analyses, in: 15th World Conference on Earthquake Engineering (15WCEE). Lisbon, Portugal, 24-28 September, 2012.

Wang, Z.: A Clear Definition of Seismic Hazard and Risk: A Basis for Hazard and Risk Assessment, Communication, and Management, Am. Geophys. Union, 2005, S53B-1110, 2005.

Wells, D. L. and Coppersmith, K. J.: New empirical relationships among magnitude, rupture length, rupture width, rupture area, and surface displacement, Bull. - Seismol. Soc. Am., 84, 974–1002, 1994.

Wetzler, N. and Kurzon, I.: The earthquake activity of Israel: Revisiting 30 years of local and regional seismic records along the dead sea transform, Seismol. Res. Lett., 87, 47–58, https://doi.org/10.1785/0220150157, 2016.

Yagoda-Biran, G., Maiti, S. K., Wetzler, N., Nof, R. N., Pashcur, Y., and Kamai, R.: A ground-motion database for Israel with its corresponding point-source parameters, for engineering seismology applications, Seismol. Res. Lett., 92, 2679–2690, https://doi.org/10.1785/0220200477, 2021.

Zohar, M.: Temporal and spatial patterns of seismic activity associated with the Dead Sea transform (DST) during the past 3000 yr, Seismol. Res. Lett., 91, 207–221, https://doi.org/10.1785/0220190124, 2019.

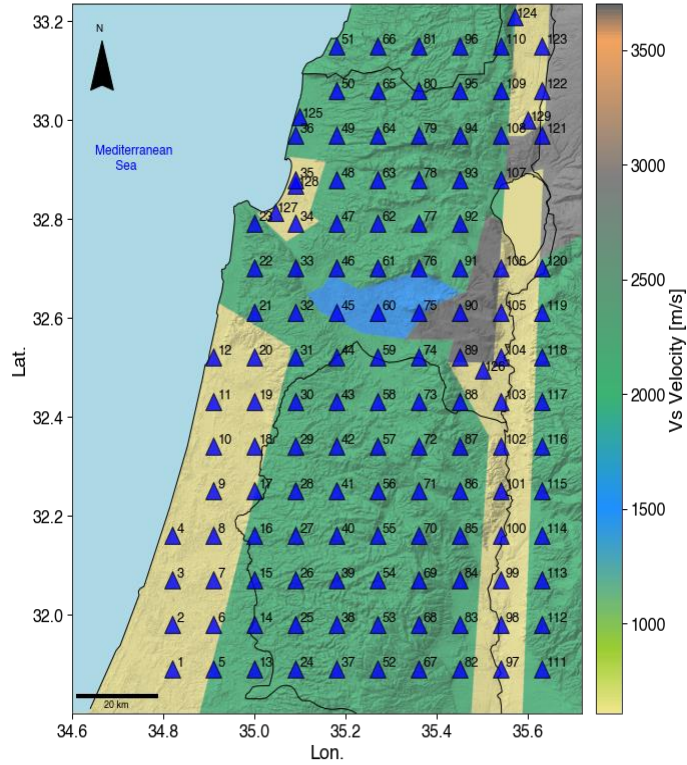## Supplementary Material

Figure 1. Numerated Synthetic stations grid (blue triangles), deployed in our model.
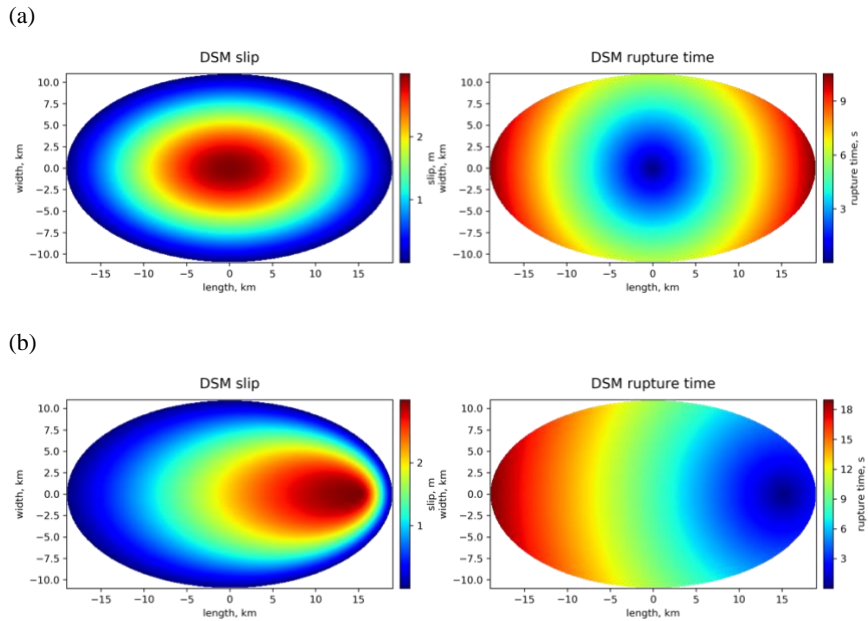
(a)

(b)

Figure 2. Examples of Rupture patches of the DSM, as used in simulating (a) symmetric and (b) southward unilateral M 7 rupture models.
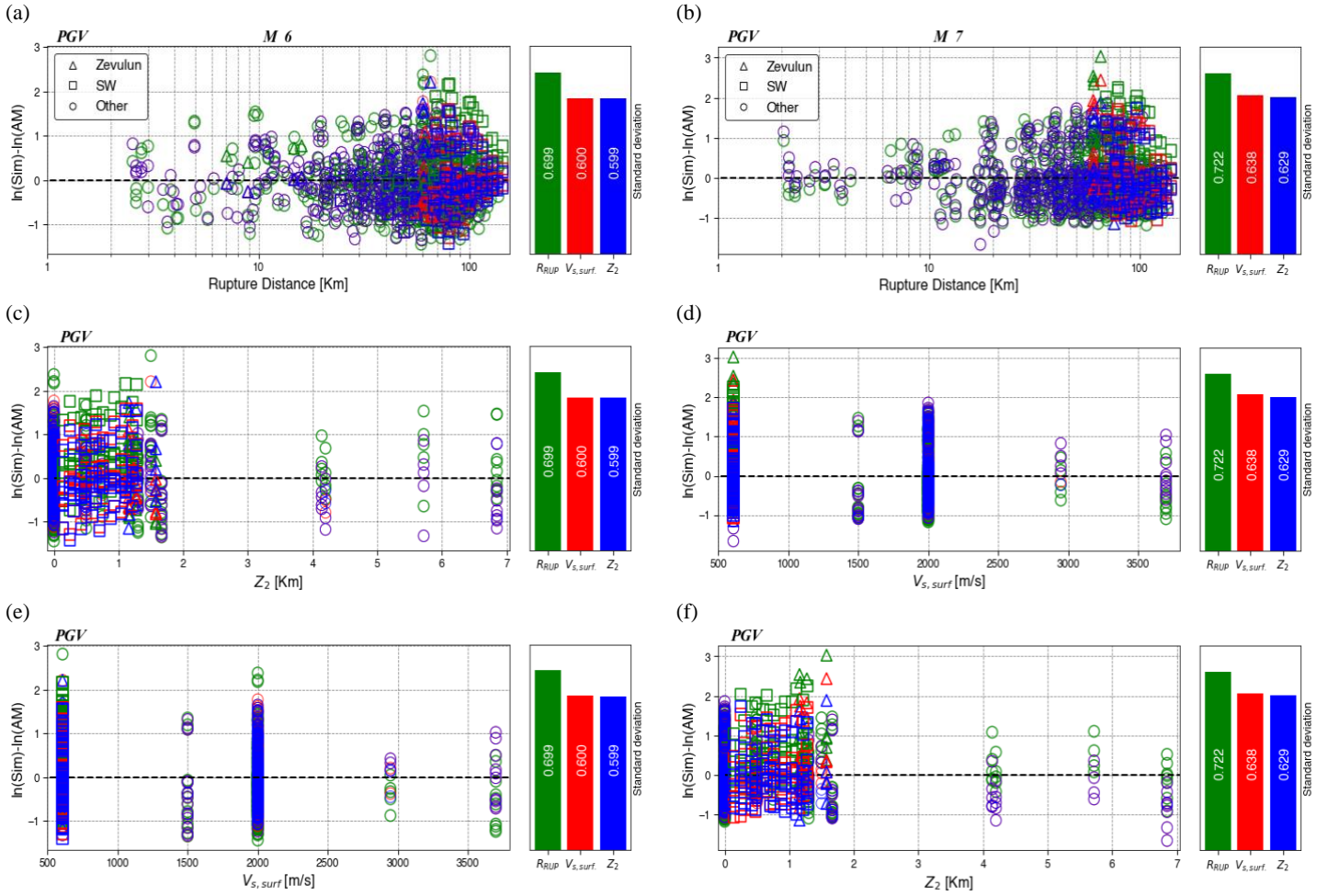
1

Figure 3. Residuals between simulated and attenuation model (AM) PGV for M 6 (left) and M 7 (right), as a function of each of the explanatory variables; (a) and (b) rupture distance (R_{RUP}), (c) and (d) surface shear wave velocity ($V_{S, surf}$), (e) and (f) depth to Vs = 2 km/s beneath the site (Z_2). The green, red and blue colors correspond to the residual's standard deviation, evolving with each added explanatory variable (green- R_{RUP}, red- R_{RUP} and $V_{S, surf}$, blue- R_{RUP}, $V_{S, surf}$ and Z_2). The records from Zevulun valley and the Sedimentary wedge marked with triangles and rectangles respectively. The other records marked with circles.
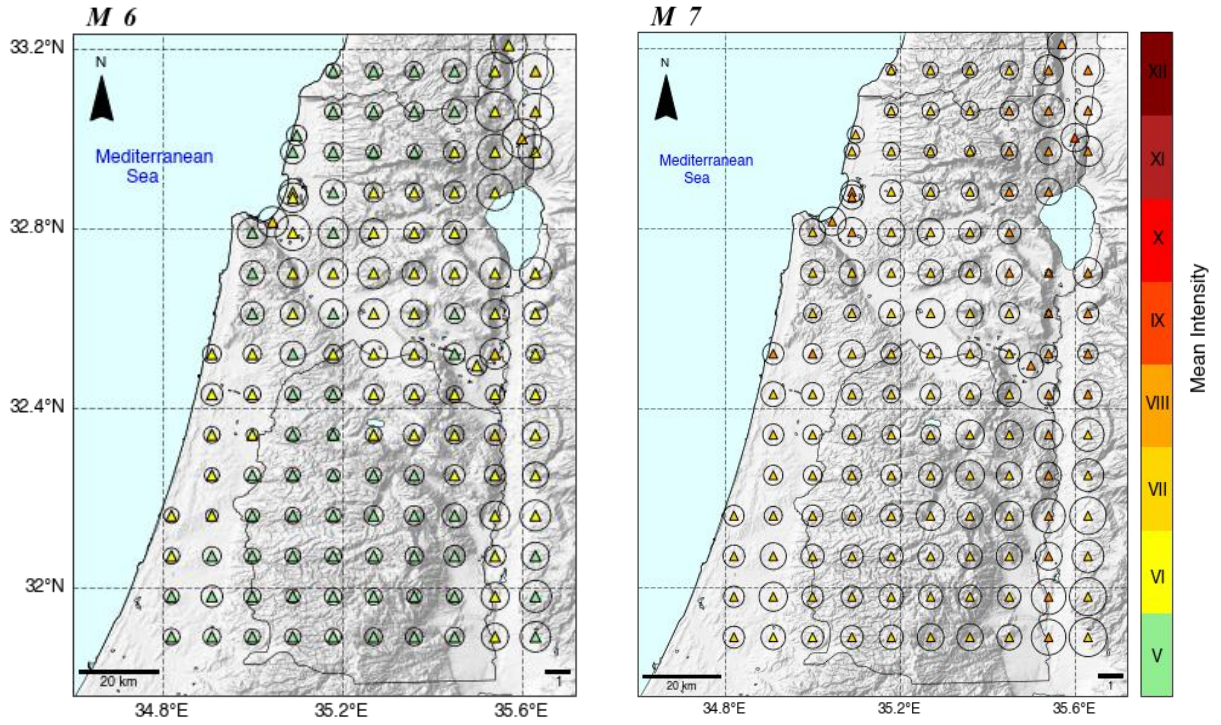
Figure 4. Map view of simulated mean EMS intensity calculated according to Kaestli & Fäh, (2006) and rounded off to the nearest integer (triangles) for M 6 (left) and M 7 (right) and their standard deviation (diameter of the circles) at each station.